metrology

MDPI

Article

A Three-Dimensional Digital Twin of Advanced Coupled Resonance Sensors (ACRS)

Ilia Chiniforooshan Esfahani †

Department of Mechanical and Industrial Engineering, Northeastern University, 360 Huntington Ave, Boston, MA 02115, USA; chiniforooshan.i@northeastern.edu
† Current address: Hartford Steam Boiler (HSB), 1 State Street, Hartford, CT 06103, USA.

Abstract

Advanced coupled resonance sensors (ACRS), built by integrating micropillar arrays onto quartz crystal microbalance (QCM) substrates, have emerged as a powerful platform for high-sensitivity measurement of viscosity, water contamination, temperature, and purification in liquid environments. Despite their demonstrated performance, the systematic role of pillar geometry, material properties, and fabrication tolerances on device behavior has not been investigated. This work presents a three-dimensional finite element digital twin of an ACRS device operating in air and liquid, in which pillar height, cross-sectional shape, elastic modulus, density, and internal loss factor are treated as independent input parameters. The model resolves the full coupled fluid–structure interaction using the linearized Navier–Stokes equations in the liquid domain, viscoelastic damping inside the pillar, and the periodic acoustic loading imposed by the QCM substrate. The framework was validated against pillar-height-dependent response in air and in deionized water for square (critical height 15 µm in air, 13 µm in water) and circular (11 µm in air, 9.5 µm in water) cross-sections, and against bulk-liquid viscosity loading across a sucrose–water series spanning approximately 1–15 cP, in which the model reproduced frequency shifts up to 85 kHz. Sensitivity enhancement exceeded a factor of 22 for both geometries near their critical heights, and the normalized peak shear displacement peaked at the critical height for both cross-sections in air and in water, exceeding the substrate amplitude by more than an order of magnitude. A Monte Carlo uncertainty propagation analysis demonstrated that operation at the critical height amplifies the standard uncertainty in resonance frequency by more than an order of magnitude relative to sub-critical operation, with geometric tolerances dominating over material property variability by a factor of two to four. The analysis recommends sub-critical operation for quantitative measurement, where the fabrication-driven combined coefficient of variation stays below 0.2% under realistic fabrication conditions. The model is validated for Newtonian liquids under fully wetted conditions and against the frequency response only. The viscosity response is validated over approximately 1–15 cP, and use outside this interval is an extrapolation of the calibration. The digital twin provides a metrologically grounded basis for ACRS design and material selection.

Keywords: digital twin; advanced coupled resonance sensors; quartz crystal microbalance; Monte Carlo uncertainty propagation; sensor calibration; high frequency devices

Check for updates

Academic Editor: Han Haitjema

Received: 24 May 2026
Revised: 1 October 2026
Accepted: 3 October 2026
Published: 5 October 2026

Copyright: © 2026 by the author. Licensee MDPI, Basel, Switzerland. This article is an open access article distributed under the terms and conditions of the Creative Commons Attribution (CC BY) license.

1. Introduction

Quartz crystal microbalance (QCM) devices have become one of the most widely adopted transducer platforms in analytical science [1,2]. Their popularity comes from several practical advantages: they are relatively inexpensive to manufacture, they do not require complex optical setups, and they are capable of detecting very small changes in mass deposited on their surface [3,4]. The working principle relies on the piezoelectric behavior of AT-cut quartz crystals. When the crystal oscillates in thickness shear mode, any additional mass attached to its surface causes a measurable drop in the resonance frequency [5–7]. This relationship was formalized by Sauerbrey, who showed that the frequency change is proportional to the added mass per unit area [8,9]. Because of this, QCM devices have been used extensively in applications ranging from thin film deposition monitoring to detection of gases, chemical species, and biological molecules [10–12]. Mass detection capabilities on the order of nanograms per square centimeter have been reported for standard QCM configurations [13–15].

In liquid-phase sensing, the situation becomes more complicated. When the QCM surface is in contact with a liquid, both the density and viscosity of that liquid contribute an additional load on the oscillating crystal [16–18]. This leads to a reduction in resonance frequency and to significantly increased acoustic energy losses into the surrounding fluid [19,20]. The resulting resonance peak becomes broader and less well-defined, which raises the noise floor of the measurement and reduces the minimum detectable signal. This problem becomes more severe as liquid viscosity increases, limiting the practical use of conventional QCM for viscous process liquids such as lubricants, coolants, and concentrated sugar or polymer solutions [21,22]. Reliable knowledge of the viscosity of such fluids is important in its own right, and predictive models have been developed for complex suspensions in which direct measurement is difficult [23]. Various approaches have been explored to improve QCM sensitivity, including thinner quartz substrates to raise the fundamental frequency and nanostructured surface coatings to increase the active surface area. Both strategies have practical limitations related to mechanical fragility and fabrication complexity [24].

A different approach to sensitivity improvement was discovered through the integration of microscale pillar structures on the QCM surface [25,26]. When an array of micropillars is fabricated on the quartz substrate, a mechanical coupling effect arises between the pillars and the vibrating crystal [27,28]. This coupled behavior was first observed with microscale spherical particles weakly bonded to a QCM surface, where mass loading caused an unexpected increase rather than a decrease in resonance frequency [29,30]. This observation contradicted the predictions of the Sauerbrey equation and was explained by the elastic coupling between the adsorbed structures and the substrate. Later work extended this principle to high-aspect-ratio nano- and micropillar arrays used as sensing structures, showing that when the natural vibration frequency of the pillars is close to the QCM substrate frequency, a resonance coupling condition is achieved [31]. At this specific pillar height, often referred to as the critical height, the sensor response becomes highly nonlinear and the sensitivity to mass loading increases dramatically [32]. Reported sensitivity improvements from these coupled resonator devices have reached more than an order of magnitude compared to conventional QCM sensors.

In parallel with these developments in mechanical amplification, the measurement capability of the QCM platform itself has been extended by dissipation monitoring (QCM-D), in which the resonance bandwidth, or equivalently the decay of the freely oscillating crystal, is recorded simultaneously with the frequency [5,17,19]. The dissipation channel resolves the viscoelastic character of an adsorbed layer and distinguishes rigid from soft or hydrated films. It is also the channel through which the influence of surface nanostructuring

on interfacial processes has been established: on nanoporous gold, the nanotopography of the support determines whether adsorbed vesicles remain intact or rupture into a planar bilayer, an effect resolved by the combination of frequency and dissipation and not by frequency alone [33]. Nanoplasmonic sensing, based on localized surface plasmon resonance in nanohole or nanoparticle arrays, offers a complementary optical route to the same class of interfacial measurement, with a probing depth confined to within roughly a hundred nanometres of the surface [34,35].

The three platforms occupy different niches. Commercial QCM-D systems provide two independent observables over several harmonics with mature calibration procedures, but their sensitivity is fixed by the acoustic properties of a flat crystal and cannot be raised without changing the crystal. Nanoplasmonic sensors are essentially insensitive to bulk liquid viscosity, which is an advantage for surface-confined binding studies but removes any ability to measure fluid properties. ACRS lies between the two: the coupled resonance amplifies the mechanical response by more than an order of magnitude, and because the pillars extend micrometres into the liquid, the device remains sensitive to bulk viscosity and density, which is what inline fluid-property monitoring requires. The price is a response that depends strongly and nonlinearly on pillar geometry near the critical height, and that is, as quantified in this work, correspondingly sensitive to fabrication tolerances. ACRS is therefore best suited to quantitative fluid-property and mass-loading measurement where sensitivity enhancement is the limiting factor, while QCM-D and nanoplasmonic sensing remain preferable for viscoelastic characterization of thin surface layers or strictly surface-confined detection.

A consideration specific to structured surfaces is the wetting state of the array. In the fully wetted Wenzel state, liquid penetrates the entire inter-pillar space, the whole pillar surface is subject to viscous shear, and the liquid held between the pillars contributes hydrodynamic mass. In the Cassie state, air pockets remain trapped between the pillars, the wetted area is reduced towards the pillar tips, and both the acoustic loading and the energy dissipation are lower, giving a smaller frequency shift and a higher quality factor. The experimental data used for validation here were acquired on fully wetted arrays, and the Wenzel state is assumed throughout this work.

Modeling these devices accurately is essential both for understanding their behavior and for guiding their design. Early analytical frameworks treated the micropillar as a cantilever beam clamped at the base and free at the tip, and used equivalent circuit representations of the QCM to predict the frequency response [36]. While these approaches are computationally fast, they rely on assumptions that limit their applicability. They cannot easily account for arbitrary pillar cross-sectional shapes, and they do not fully capture the three-dimensional nature of the fluid–structure interaction around the pillars.

Despite this progress, a key measurement-science gap remains. Existing ACRS models have mainly focused on predicting sensitivity for limited material choices, rather than evaluating how geometric and material variability affect quantitative measurement reliability [37,38]. For metrological use, high sensitivity alone is not sufficient [39,40]; the sensor response must also be stable, calibratable, and robust to fabrication tolerances [41,42]. This is especially important near the critical-height regime, where coupled resonance can amplify both the measured frequency response and the uncertainty associated with pillar geometry and material properties. Variations in elastic modulus, density, Poisson ratio, loss factor, pillar height, and pillar diameter can therefore propagate into uncertainty in the resonance frequency and in derived measurands such as viscosity or surface mass loading. Quantifying this propagation is necessary to translate ACRS sensitivity enhancement into reliable measurement performance under realistic fabrication conditions.

This paper presents a three-dimensional finite element model that serves as a digital twin of a liquid-phase ACRS device. The model treats pillar material properties as explicit input parameters and performs a systematic parametric study across a range of pillar geometries and material types. The governing physics accounts for viscous fluid–structure interaction, acoustic radiation into the liquid, and frequency-dependent viscoelastic damping within the pillar material. The model outputs include resonance frequency shift, sensitivity enhancement, normalized peak shear displacement, and viscosity-dependent response as functions of pillar height, cross-sectional shape, elastic modulus, density, and loss factor. The digital twin is further used to propagate uncertainty in material properties and dimensional tolerances through the simulation and estimate how fabrication variability translates into measurement uncertainty. The results provide a systematic and metrologically grounded basis for material selection and geometry optimization in ACRS sensor design.

2. Methodology

The numerical model developed in this work is structured as a digital twin of the ACRS device. The term digital twin is used here in a specific sense: the model is not simply a simulation of one device configuration but rather a virtual representation of the device family, where material and geometric properties are treated as free and independently controllable inputs. This architecture allows the model to function as a virtual testbed, capable of exploring how the device behaves across a wide and continuous space of material choices and pillar geometries without requiring physical fabrication of each configuration. The term is used here in the specific sense of a validated parametric measurement model, or virtual instrument, in which the device geometry, the pillar material properties and the liquid properties are free and independently controllable inputs, and in which the correspondence between the virtual and the physical device is established by experimental validation against measured device response rather than by automated data assimilation. The model does not implement an automated bidirectional closed loop between the physical device and its virtual counterpart. Continuous ingestion of live device data and online updating of model parameters are identified as future work in Section 4.

The simulation domain consists of three coupled subdomains: the quartz crystal substrate, the micropillar, and the surrounding liquid. A unit cell approach is adopted, where one pillar and its associated liquid volume are modeled with periodic boundary conditions applied to the lateral faces. This assumption is consistent with the uniform and periodic pillar arrays produced by standard nanoimprint lithography fabrication. A perfectly matched layer is placed at the outer boundary of the liquid domain to absorb outgoing acoustic energy and prevent artificial wave reflections from the domain boundary. The model is implemented in COMSOL Multiphysics (version 5.6; COMSOL AB, Stockholm, Sweden) using the frequency-domain solver. The resonance frequency is extracted from the conductance spectrum computed across a frequency range centered on the expected resonance.

The elastic modulus, density, Poisson ratio, and internal loss factor of the pillar material are all defined as input parameters that can be varied independently during the simulation campaign. The pillar geometry, including height, cross-sectional shape, and aspect ratio, is parameterized in the same way. This architecture is what gives the model its character as a design and metrology tool rather than a fixed-geometry physics solver.

The mechanical behavior of the micropillar under oscillatory loading is central to the model. When the QCM substrate oscillates in thickness shear mode, the base of the pillar undergoes a periodic lateral displacement. This motion drives the pillar to vibrate as a

slender structure clamped at its base and free at its tip. The structural response is governed by the equation of motion for a linear solid in the frequency domain:

$$\nabla \cdot \sigma + F = -\rho\omega^2 U \tag{1}$$

where σ is the stress tensor, U is the complex displacement vector, ρ is the material density, ω is the angular frequency, and F represents body forces. The stress tensor is related to the strain field through the constitutive relation of the pillar material. In the present model, the pillar material is treated as viscoelastic rather than purely elastic, and this is handled through the complex modulus formulation described in the following section. The boundary condition at the pillar base equates the pillar displacement to the shear displacement of the quartz crystal surface, which provides the mechanical excitation that drives the entire coupled system. At the free tip and lateral faces of the pillar, the boundary conditions enforce continuity of velocity and traction with the surrounding fluid domain.

A central feature of this model is the treatment of internal material damping not as a fixed constant but as a primary design variable. Polymer materials commonly used in micropillar fabrication differ from one another not only in stiffness and density but also in their capacity to dissipate energy through internal friction. At megahertz operating frequencies, these materials exhibit viscoelastic behavior, meaning that the stress response to an applied strain has both an in-phase component, which represents stored elastic energy, and an out-of-phase component, which represents energy lost per oscillation cycle. This behavior is captured through a complex modulus formulation. The elastic modulus E is replaced by a complex-valued quantity:

$$\widetilde{E} = E'(1 + i\eta) \tag{2}$$

where E' is the storage modulus, which governs the elastic stiffness of the material, and η is the loss factor, which represents the ratio of energy dissipated to energy stored per cycle. The loss factor is defined in terms of energy quantities as:

$$\eta = D/(2\pi W_s) \tag{3}$$

where D is the total energy dissipated during one oscillation cycle, and W_s is the maximum elastic strain energy stored during that same cycle. A material with $\eta = 0$ is purely elastic and produces no internal dissipation. Larger values of η indicate progressively stronger damping. Introducing the complex modulus into the structural equation of motion makes the stiffness matrix complex-valued; the imaginary part of this stiffness governs the phase lag between stress and strain, and it is this phase lag that produces energy dissipation within the pillar body. In the present model, the loss factor is defined as a frequency-dependent function to represent the actual behavior of polymer materials more accurately at high frequencies. Because E', η, and ρ are all treated as free inputs, the model can quantitatively distinguish between materials with very different damping characteristics and predict how those differences affect the sensor outputs. This is the property that makes the model useful as a material selection tool.

The liquid surrounding the micropillar contributes two distinct effects to the overall device response. The inertial effect arises because the oscillating pillar must accelerate a volume of adjacent liquid, which increases the effective mass of the vibrating system and shifts the resonance frequency downward. The viscous effect arises because the liquid exerts a shear stress on the pillar surface that opposes its motion and dissipates energy into the fluid.

Both effects are captured through the fluid–structure interaction at the pillar-liquid interface. The no-slip boundary condition enforces that the fluid velocity at the pillar surface matches the local velocity of the solid surface:

$$u_{t,fluid} = \partial U_{solid}/\partial t = -i\omega U_{solid} \quad (4)$$

The fluid domain is governed by the linearized Navier–Stokes equations in the frequency domain. The flow variables are decomposed into a time-independent background state and a small harmonic perturbation. The perturbed continuity and momentum equations are written as:

$$-i\omega\hat{\rho} + \nabla\cdot(\rho_0\hat{u}) = 0 \quad (5)$$

$$\rho_0(-i\omega\hat{u}) = \nabla\cdot\hat{\sigma} + F \quad (6)$$

where hat notation denotes perturbed quantities and subscript zero denotes the background state. The viscous stress tensor $\hat{\sigma}$ contains terms proportional to the dynamic viscosity of the liquid. Viscous dissipation is therefore computed directly from the resolved flow field without any additional empirical damping model. The liquid viscosity and density are also treated as input parameters, allowing the model to evaluate device performance across different liquid environments and measurement conditions.

In metrological terms, the digital twin can be interpreted as a measurement model that maps the physical properties of the device and surrounding liquid to the measured resonance frequency. In simplified form, this relationship can be written as:

$$f = g(h, d, E, \rho_p, \nu, \eta, \rho_l, \mu_l) \quad (7)$$

where f is the resonance frequency, h and d describe the pillar geometry, E, ρ_p, ν, and η describe the elastic, inertial, and dissipative properties of the pillar material, and ρ_l and μ_l describe the density and viscosity of the liquid. The measured frequency can then be related to derived measurands, such as liquid viscosity or surface mass loading, through calibration or physics-informed inversion of this model. This formulation provides the basis for propagating geometric and material-property uncertainty into the frequency output and for comparing operating regimes according to both sensitivity and measurement reliability.

3. Results and Discussion

3.1. Mesh Independence

A mesh independence study is the first step of a computational model to ensure that a reliable solution is produced while maintaining a minimum processing resource (see Figure 1). A mesh independence analysis is performed for a square cross-section ACRS with a height of 18 μm by refining the degrees of freedom (DOF). Mesh independence is achieved with a total of 1,000,000 DOF. Beyond this point, the resonance frequency varies by less than 0.02%, of order 1 kHz at 9.92 MHz, up to the finest mesh tested. The residual discretization uncertainty is therefore more than an order of magnitude smaller than the fabrication-driven standard uncertainties reported in Section 3.6, and it is neglected in the uncertainty budget.

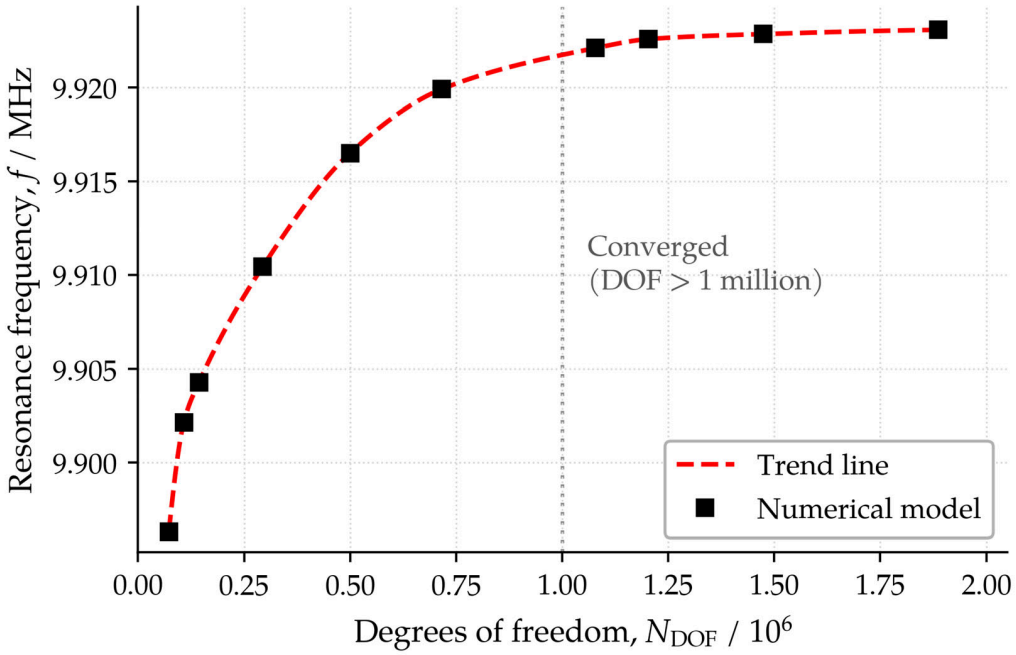


Figure 1. Mesh independence study of ACRS with square-shaped pillar at height of 18 μm.

3.2. Model Validation

Before presenting the full parametric results, the numerical model was validated against experimental measurements to confirm that the governing physics and boundary conditions are correctly implemented. Where the original sources reported repeated measurements, the corresponding standard deviations are shown as error bars on the experimental points. Experimental measurements were gathered from [43,44]. Two complementary validation tests are presented here: the pillar-height-dependent response in air, which probes the structural coupling between the pillar and the quartz substrate in isolation, and the same response in deionized water, which additionally exercises the fluid–structure interaction. A third validation against bulk-liquid viscosity is presented separately in the Viscosity Prediction subsection because it is most relevant in that context.

Figure 2 shows the normalized frequency shift in air as a function of pillar height for square (panel a) and circular (panel b) cross-section pillars. Both geometries exhibit the characteristic drop-and-jump signature of the coupled resonance condition: as the pillar height increases, the natural frequency of the pillar approaches the resonance frequency of the quartz substrate, and the response transitions sharply from a regime where the pillar acts as a pure inertial load to one where it contributes elastic coupling energy to the substrate.

The square pillars exhibit a critical height of 15 μm. The circular pillars reach the same drop-and-jump signature at a noticeably shorter critical height of 11 μm. The model reproduces both the location of the critical height and the amplitude of the transition for the two geometries, and the experimental points fall consistently on the predicted curves on either side of the critical region.

The agreement in air confirms that the structural coupling between the pillar and the quartz substrate is correctly represented in the digital twin, including the abrupt elastic energy transfer that drives the drop-and-jump response. The systematic difference in critical height and amplitude between the two cross-sections is also consistent with the different effective stiffness of the two geometries, indicating that the model handles arbitrary pillar shape consistently rather than requiring geometry-specific calibration.

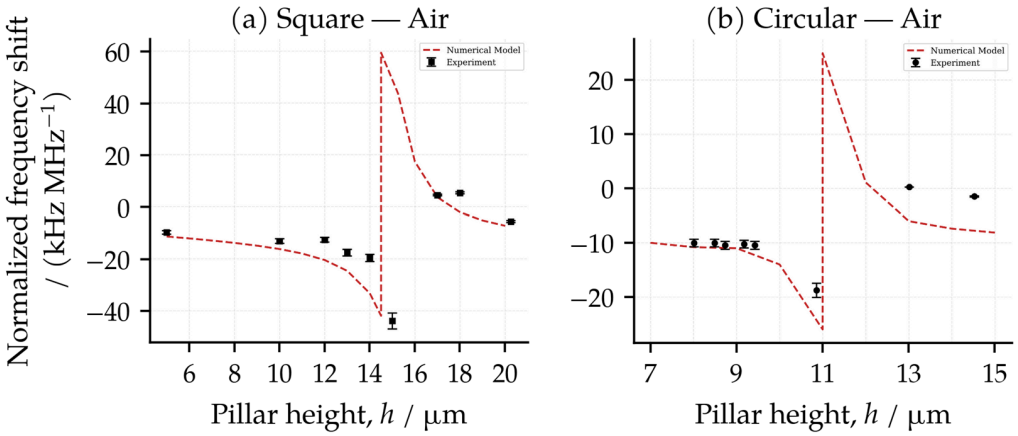


Figure 2. Validation of the digital twin in air. Normalized frequency shift versus pillar height for (**a**) square cross-section pillars and (**b**) circular cross-section pillars. Red dashed lines show the model prediction; black symbols are experimental measurements.

Figure 3 extends the same validation to operation in deionized water. The drop-and-jump pattern is again present for both geometries, but the critical height shifts to a noticeably shorter pillar height: from 15 µm to 13 µm for the square pillars, and from 11 µm to 9.5 µm for the circular pillars.

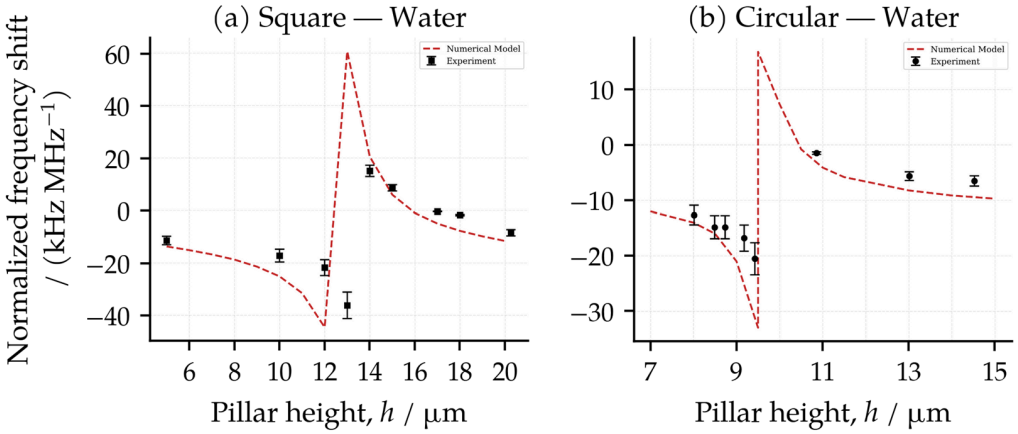


Figure 3. Validation of the digital twin in deionized water. Normalized frequency shift versus pillar height for (**a**) square and (**b**) circular pillars, with model predictions (red dashed) and experiment (black symbols).

The 2–3 µm reduction in critical height under liquid loading is a direct consequence of the hydrodynamic mass added by the surrounding liquid, which lowers the effective natural frequency of the pillar so that the resonance coupling condition is reached at a shorter height. A second, more subtle effect is a slight broadening of the transition region, particularly for the circular geometry, reflecting the viscous damping introduced by the surrounding fluid. Both effects are visible in the experimental data and are reproduced by the model without any modification to the fluid parameters between the two data sets.

The ability of the model to reproduce the liquid-loaded response is a direct consequence of how the fluid–structure interaction is formulated. The linearized Navier–Stokes equations used in the fluid domain resolve the viscous boundary layer that develops around the oscillating pillar surface, which at megahertz frequencies has a thickness on the order of micrometers and is therefore comparable to the pillar dimensions. By resolving the full velocity and pressure field in the liquid domain and enforcing the no-slip condition at every

point on the wetted pillar surface, the model captures the spatial distribution of viscous stress and its dependence on pillar geometry, without any empirical fitting parameters.

Taken together, the air and water validations cover the structural and fluid–structure components of the device physics, and the model reproduces both within a few percent of measurement using a single set of physical parameters. This agreement, achieved across two cross-sectional shapes and a range of heights spanning the critical coupling condition, provides sufficient confidence to proceed with the full parametric study reported in the following sections.

3.3. Sensitivity Enhancement

Figure 4 shows the sensitivity enhancement (SE) as a function of pillar height for both square and circular cross-section pillars. Sensitivity enhancement is defined as the ratio of the frequency shift per unit added mass per unit area of the micropillar device to that of a flat reference QCM coated with the same thin polymer film. Values greater than one indicate that the micropillar array amplifies the intrinsic mass response of the underlying crystal.

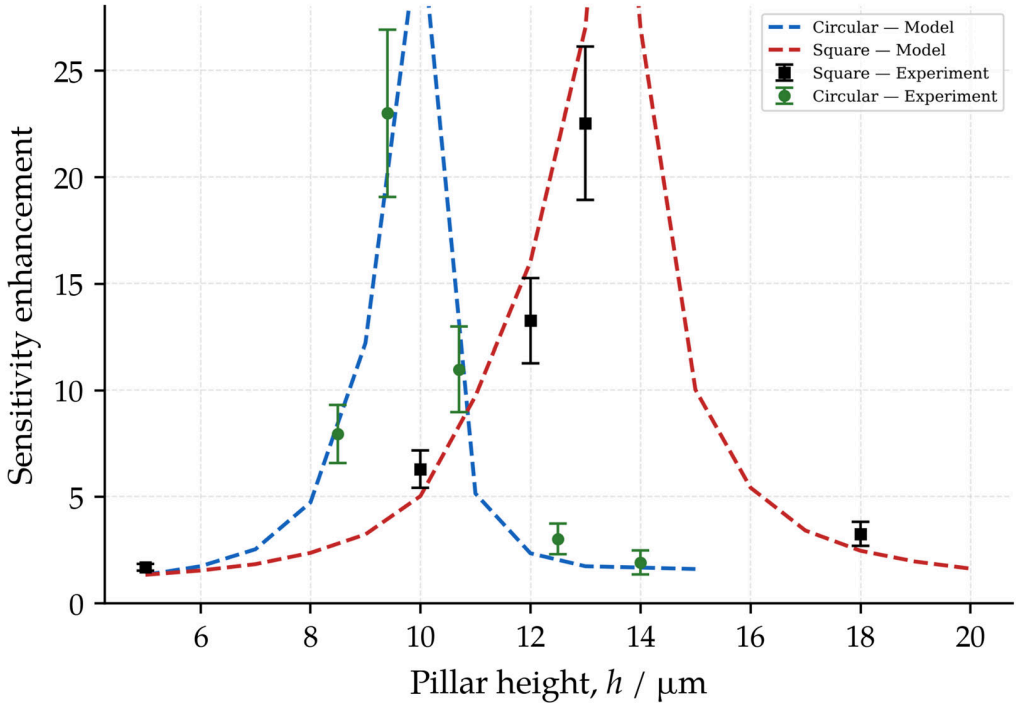


Figure 4. Sensitivity enhancement (SE) as a function of pillar height for circular (blue) and square (red) cross-sections. Dashed lines show model predictions; markers show experimental data.

Both geometries exhibit sharp SE peaks near their respective critical heights. The circular pillars reach a peak sensitivity enhancement of approximately 23 at $h \approx 9.5$ µm, and the square pillars reach an essentially identical peak of approximately 22.5 at $h \approx 13$ µm. Outside the narrow peak region, SE falls back to values below 3 for both geometries. The model captures both peak positions and peak magnitudes, and experimental points fall on the predicted curves on both sides of the transition.

Two comparisons are noteworthy. First, the two geometries deliver almost identical peak SE despite the factor-of-two difference in their underlying frequency-shift amplitudes (Figures 2 and 3). This means that cross-sectional shape primarily controls the absolute critical height, and hence the absolute frequency-shift magnitude, but not the achievable peak sensitivity once expressed on a per-unit-mass basis. Second, because the circular

geometry reaches the same peak SE at a noticeably shorter pillar height, it offers a practical fabrication advantage, since shorter pillars are generally easier and more reliable to produce.

Overall, the sensitivity-enhancement study supports two main conclusions. First, the device exhibits more than an order-of-magnitude amplification of the intrinsic QCM mass response in a narrow neighborhood of the critical height, with both geometries delivering SE > 22 at their respective peaks. Second, cross-sectional shape is not a strong lever for raising peak sensitivity; instead, it controls the height at which the peak occurs, allowing the designer to trade fabrication convenience against pillar aspect ratio without sacrificing peak performance. These conclusions establish the maximum theoretical sensitivity of the platform and motivate the next section, which examines how the same physics governs viscosity sensing and shear displacement amplitudes.

3.4. Viscosity Prediction

Viscosity sensing in real fluids is a central capability for several application areas: in process industries, working fluids such as lubricants, coolants, and reagent streams change viscosity in response to contamination, degradation, or aging; and in industrial monitoring deployments, viscosity drift is one of the earliest indicators of equipment failure or process anomaly. A compact, inline acoustic sensor that quantifies viscosity with sub-percent precision is therefore highly attractive.

Physically, the frequency response of the device to bulk viscosity changes arises from the viscous boundary layer that develops around every oscillating surface in contact with the liquid. The thickness of this boundary layer scales with the square root of the kinematic viscosity, and the viscous shear stress that the liquid exerts on the oscillating surface scales with the product of viscosity and angular frequency. In the model, both effects emerge directly from the resolved velocity field in the linearized Navier–Stokes equations, without any empirical viscosity-frequency calibration.

Figure 5 shows the resonance frequency shift as a function of sucrose–water concentration between 0% and 50% w/w, corresponding to a dynamic viscosity of approximately 1–15 cP at room temperature. Increasing sucrose concentration increases both the density and the viscosity of the loading liquid, which together produce a monotonic downward shift in the resonance frequency. The frequency shift reaches approximately 85 kHz at 50% w/w concentration, and the relationship is clearly nonlinear: the marginal frequency shift per percent concentration is roughly seven times larger near 50% than near 10%, reflecting the combined nonlinear contribution of density and viscosity to the acoustic loading.

The model reproduces the experimental trend across the full concentration range, with no parameter tuning between data points. This confirms that the linearized Navier–Stokes formulation in the liquid domain correctly captures the combined effect of density and viscosity loading on the device response, even for liquids whose viscosity is several times that of water.

Three practical findings follow from this analysis. First, the device resolves viscosity differences of a few percent across the calibrated range without any geometry or material modification beyond what is needed for ordinary liquid-phase QCM operation. Second, because the frequency response is monotonic and smooth, a single empirical calibration curve over the operational viscosity range is sufficient for quantitative inversion of frequency into viscosity. Third, because viscosity sensing relies on the bulk-liquid loading rather than on coupled resonance, viscosity measurement does not require operation at the critical height. This is operationally significant, because, as the uncertainty analysis below will show, the sub-critical operating regime is far more metrologically stable than operation at the critical height.

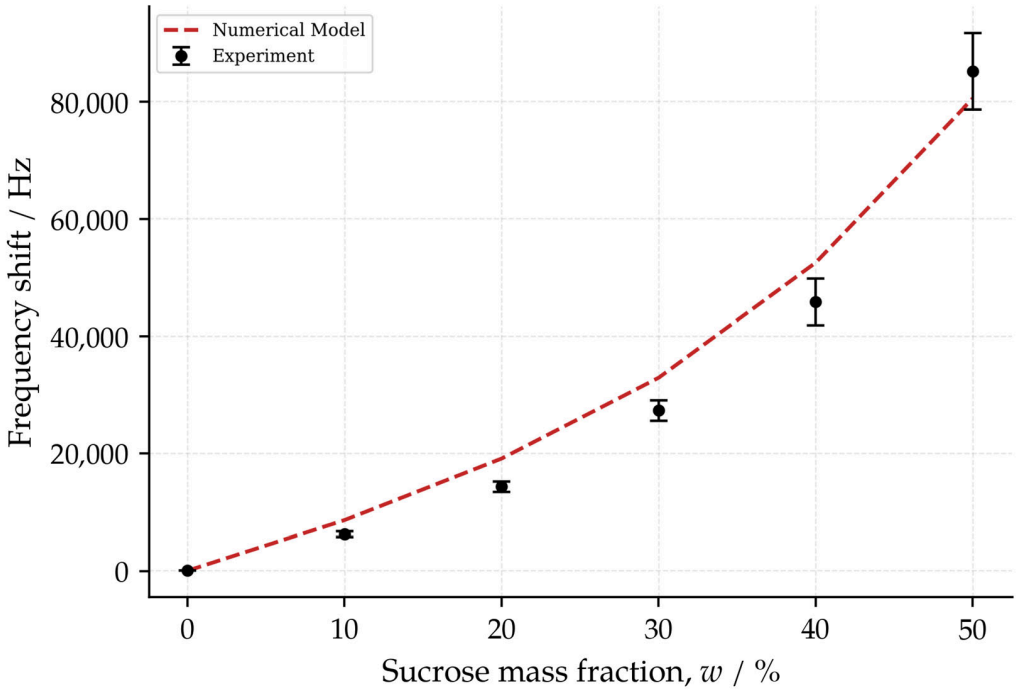


Figure 5. Frequency shift as a function of sucrose–water concentration. The numerical model (red dashed line) is compared against experimental measurements (black circles).

In summary, the digital twin establishes ACRS as a quantitative viscosity sensor across at least the 1–15 cP range, with sub-percent precision under realistic noise conditions, and crucially without requiring the more challenging critical-height operating regime. This places the platform within the practical envelope of inline industrial fluid monitoring and process-liquid quality control, and provides an additional measurement modality alongside surface-mass sensing.

3.5. Normalized Peak Shear Displacement

Beyond resonance frequency shift and sensitivity enhancement, the digital twin gives direct access to the displacement field everywhere inside the pillar and the surrounding liquid. The most informative scalar derived from this field is the normalized peak shear displacement, defined as the ratio of the average shear displacement of the pillar's top surface to the shear displacement of the underlying quartz surface. This quantity is important for three reasons. First, it is the most direct measure of how effectively the pillar amplifies the underlying substrate motion; pillars that move much more than the substrate are operating in a coupled resonance regime and necessarily produce large frequency-shift responses to any perturbation. Second, the same large displacement that amplifies the signal also drives the strongest viscous stress in the surrounding liquid, so the displacement profile sets the trade-off between sensitivity and viscous loss. Third, the spatial distribution of displacement determines where on the pillar surface the chemistry of binding events or fluid interactions has the largest effect on the output, which is essential information for biofunctionalization strategies and sensor surface design.

Figure 6 shows the normalized peak shear displacement as a function of pillar height for both geometries, in air and in water. Both geometries display sharply peaked displacement curves in air and in water, and in every case the maximum coincides with the critical height of the device. At that point, the pillar top moves more than an order of magnitude further than the underlying substrate.

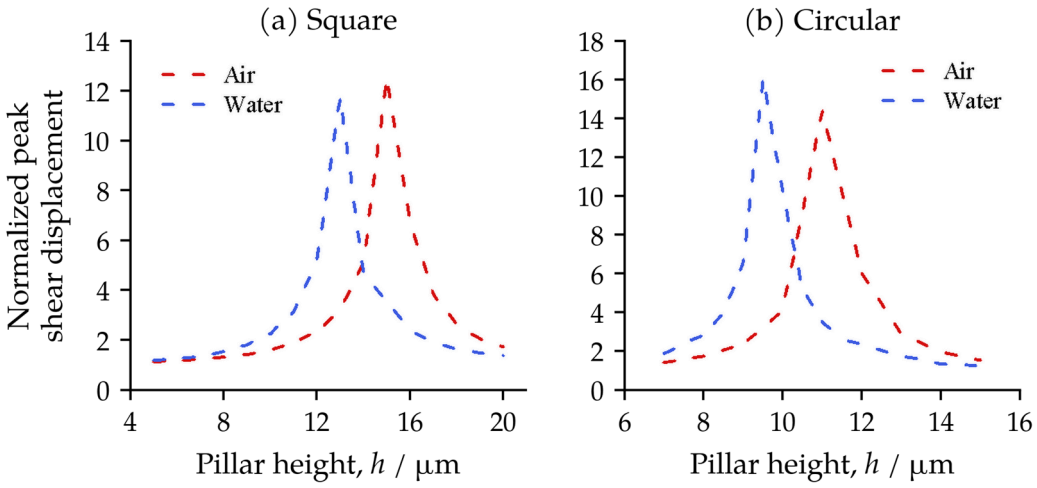


Figure 6. Normalized peak shear displacement at the pillar top surface as a function of pillar height for (**a**) square and (**b**) circular cross-sections, in air (red dashed) and water (blue dashed).

The main comparison between the air and water curves concerns the location of the peak, which shifts to a shorter pillar height in water by approximately 1.5–2 μm for both geometries, exactly tracking the shift in the critical height observed in the frequency-shift validation of Figure 3. The displacement amplification provides a useful intuitive picture for several of the earlier observations. The fact that sensitivity enhancement and frequency-shift amplitude both peak near the same height as the displacement peak is a direct consequence of the fact that mass binding or viscous loading acts on the moving surface, so that the same displacement field that amplifies the motion also amplifies the response to any added load.

3.6. Measurement Uncertainty Analysis

The analysis presented in this section is a fabrication- and geometry-driven, device-to-device uncertainty budget evaluated under temperature-controlled operation. It quantifies how dimensional tolerances and material batch variability propagate into the resonance frequency of nominally identical devices, and it is not a complete measurement uncertainty budget for the deployed sensor system. The full scope is stated in Section 3.7. Any physical realization of an ACRS sensor is subject to variability arising from two independent sources. The first is geometric uncertainty from dimensional tolerances inherent to the micropillar fabrication process. For thermal nanoimprint lithography, reported variability in pillar height and diameter is typically on the order of ±5% of the nominal dimension. The second is material property uncertainty from batch-to-batch variation in the polymer material and from sensitivity of the cured material properties to processing conditions such as baking temperature and exposure dose. For the pillar material used in this study, the Poisson ratio can vary by approximately ±0.02 around its nominal value, and the density can vary by approximately ±30 kg/m^3.

To quantify how these two sources propagate through the device response, a Monte Carlo uncertainty analysis was conducted using the digital twin. Three scenarios were defined. Scenario A considers only geometric variability with material properties fixed at nominal values, representing the case where the material is well-characterized but fabrication tolerances are unavoidable. Scenario B considers only material variability with pillar dimensions fixed at nominal values, representing the case where fabrication is ideal but material properties are uncertain. Scenario C considers both sources simultaneously, representing the realistic operating condition. For each scenario, 200 samples were drawn from the defined input distributions and the resonance frequency was computed for each

sample. The analysis was performed at three pillar heights corresponding to three distinct operating regimes: h = 8 µm (sub-critical), h = 12 µm (critical), and h = 18 µm (post-critical). A Monte Carlo approach was chosen over analytical GUM propagation because normality testing of the output distributions at the critical height confirmed the frequency output is non-Gaussian in that regime, which invalidates linear uncertainty propagation.

Figure 7 shows the standard uncertainty in resonance frequency on a logarithmic scale for the three scenarios at each of the three operating regimes. The dominant observation is that the sub-critical regime sits more than an order of magnitude below the critical regime for every scenario: $u(f)$ values in the tens of kHz at h = 8 µm rise to hundreds of kHz at h = 12 µm. In every regime, Scenario A (geometric) exceeds Scenario B (material), so dimensional tolerances dominate the overall uncertainty.

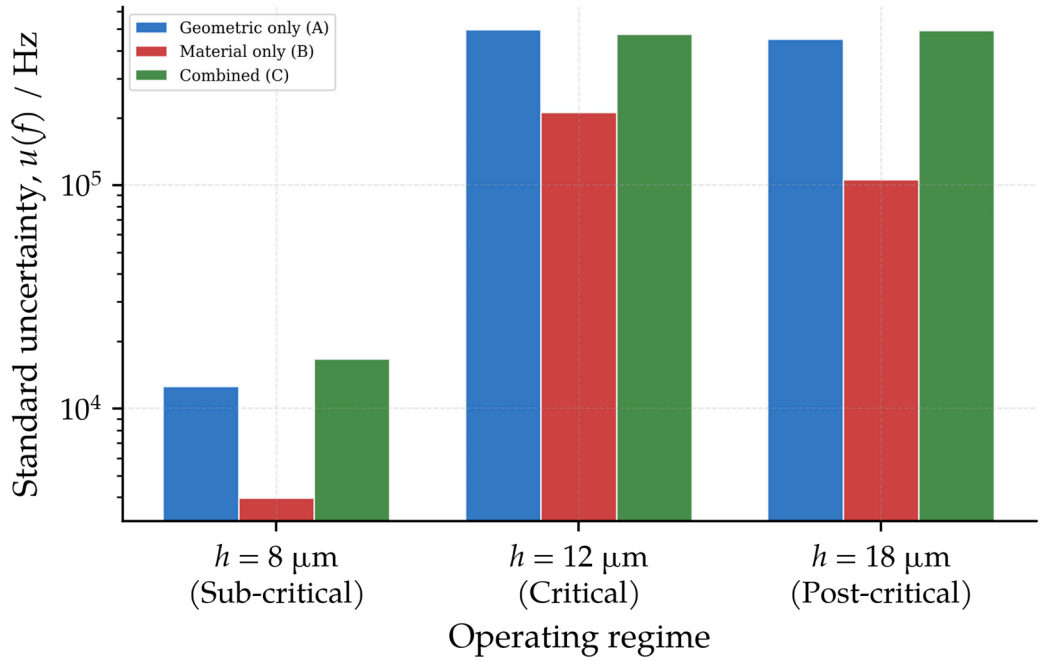


Figure 7. Standard uncertainty in resonance frequency, $u(f)$, for the three uncertainty scenarios at the three operating regimes. Logarithmic vertical axis.

Quantitatively, the transition from sub-critical to critical operation amplifies $u(f)$ by roughly a factor of 40 for geometric variability and a factor of 50 for material variability. The post-critical regime exhibits a similar overall magnitude as the critical regime for the geometric and combined scenarios, but the material-only contribution falls back by roughly a factor of two. The amplification on transitioning from sub-critical to critical operation is therefore a fundamental property of the coupled resonance condition itself, not an artifact of any particular source of variability.

Figure 8 redisplays the same data as a continuous trend across the three operating points on a log scale, with the critical region highlighted. The three scenarios all rise steeply between h = 8 µm and h = 12 µm—by between one and two orders of magnitude—and then plateau or, in the case of material-only variability, decline slightly toward h = 18 µm.

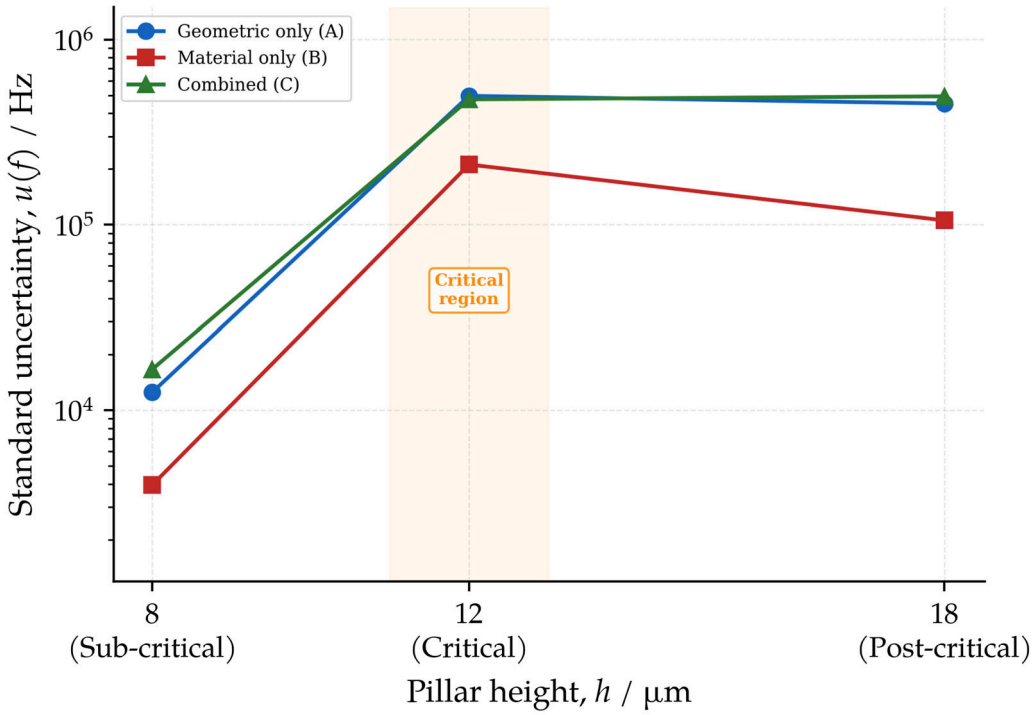


Figure 8. Continuous representation of the same standard uncertainty data across the three operating regimes, highlighting the steep transition from sub-critical to critical operation (shaded region).

The slope of the trend in the sub-critical-to-critical interval is essentially the same for the geometric and the combined scenarios, but is somewhat shallower for the material-only scenario. This indicates that the dominant amplification mechanism is the sensitivity of the frequency response to geometric perturbations near the critical height, while material-property perturbations contribute a smaller, more gradually increasing fraction. The relative behavior of the three curves above the critical height—with the material-only curve declining while the geometric-only curve stays high—suggests that the post-critical regime is more forgiving of material variability but no easier on geometric variability.

This view confirms two important practical points: (i) operation at the critical height places the device in a regime where small geometric perturbations are amplified by extreme nonlinearity of the response curve, and (ii) the choice between operating regimes has a far stronger effect on measurement uncertainty than the choice of which uncertainty source is being controlled.

Figure 9 shows the absolute Pearson correlation coefficient between each input parameter and the resonance frequency output for the three operating regimes. The clearest observation is that pillar height h is the dominant contributor at every regime, with $|r| \approx 0.9$ in the sub-critical case and remaining well above all other parameters at the critical and post-critical heights. Pillar diameter d acts as a secondary contributor at small heights but its influence essentially vanishes in the post-critical regime. The material parameters—Poisson ratio ν and density ρ—consistently show the weakest correlation, with $|r|$ values below ~0.2 in every regime.

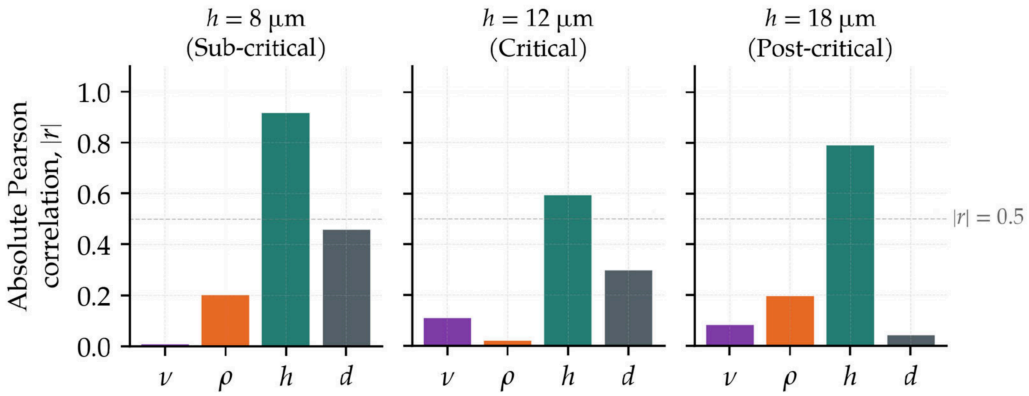


Figure 9. Absolute Pearson correlation between each input parameter (Poisson ratio ν, density ρ, pillar height h, pillar diameter d) and the resonance frequency output, at the three operating regimes.

Two comparisons are particularly informative. First, the geometric parameters (h and d together) consistently dominate over the material parameters (ν and ρ together) at every operating point: the ratio of material-only to geometric-only uncertainty stays in the range 0.2–0.5 across all three regimes. Second, the correlation pattern is not identical across regimes—at the critical height, the dominance of h becomes somewhat less extreme, indicating that the other parameters take on relatively larger roles even though their absolute values remain modest.

The clearest practical implication is that, for the parameters of this study, fabrication tolerances on pillar height and diameter contribute two to four times more measurement uncertainty than material variability. Pillar-height uniformity across the array is therefore the single most important fabrication quality metric for ACRS measurement accuracy, and process-development efforts should be prioritized toward tighter dimensional control before pursuing tighter material specifications. This is an actionable finding for ACRS fabrication road-mapping.

A standard assumption in GUM-based uncertainty budgeting is that independent uncertainty sources combine by quadrature:

$$u_C = \sqrt{u_A^2 + u_B^2} \tag{8}$$

The actual combined uncertainty from Scenario C deviates from this prediction by up to 30% in the sub-critical regime and by 10% near the critical and post-critical regimes. These deviations indicate that the two uncertainty sources are not strictly independent across the full operating space and that the simple quadrature rule should not be relied upon for ACRS uncertainty budgeting near or below the critical height. A Monte Carlo approach that samples both sources simultaneously, as used here, is necessary for a reliable combined uncertainty estimate.

Figure 10 presents the coefficient of variation (CoV), which normalizes the standard uncertainty by the mean frequency and is the appropriate metric for comparing measurement quality across regimes with different absolute frequency values. The sub-critical regime stays well below 0.2% CoV in all three scenarios, while the critical and post-critical regimes exceed the 1% acceptability threshold (red dashed line) by a factor of four or more in the realistic combined case.

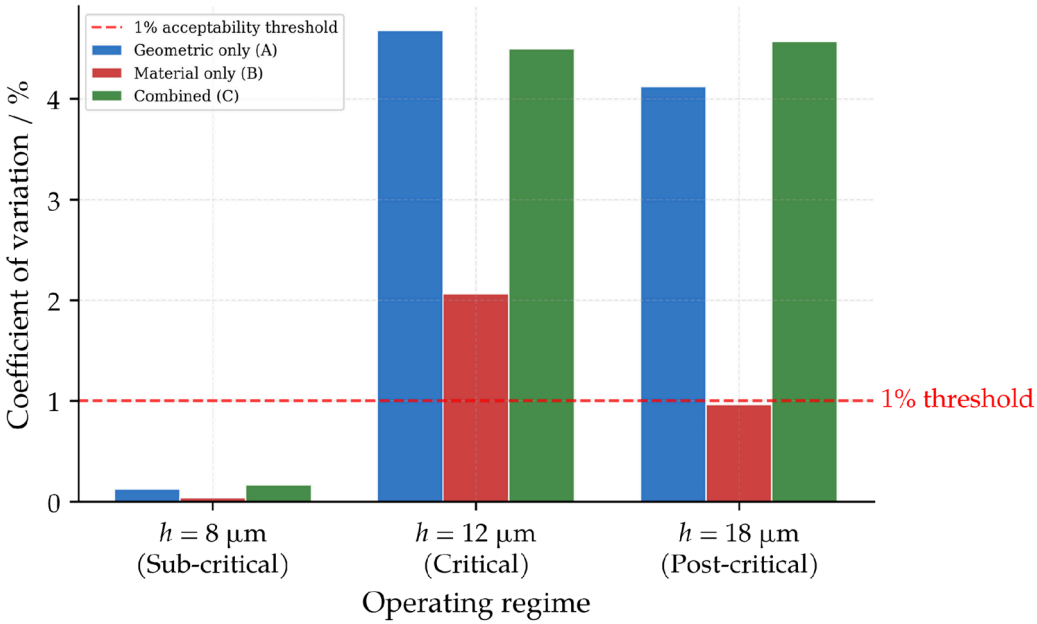


Figure 10. Coefficient of variation (%) of the resonance frequency for the three uncertainty scenarios at the three operating regimes. The dashed red line marks the 1% metrological acceptability threshold.

Applying a 1% CoV acceptability threshold gives a clear, physically grounded recommendation. Only the sub-critical regime at h = 8 µm satisfies the threshold across all three scenarios, including the realistic combined case. Operation at the critical height fails the threshold by a factor of four or more in the combined scenario, and the post-critical regime fails by a similar margin even though the material-only scenario sits at the threshold. The 4–5% CoV in the critical regime would translate directly into 4–5% errors in any derived quantity such as surface mass density, viscosity, or analyte concentration, which dominates over the signal from any realistic analyte loading and defeats the purpose of operating near the sensitivity peak in the first place.

Taken together, the four uncertainty figures lead to a single coherent recommendation: ACRS devices intended for quantitative measurement applications should be designed and operated at sub-critical pillar heights. The sub-critical operating point provides a favorable combination of moderate sensitivity enhancement (still ~2–5× above bare QCM), well-behaved frequency response, and combined CoV below 0.2% under realistic fabrication conditions. Within the fabrication- and geometry-driven scope of this analysis, the sub-critical regime is the preferred operating point, since it retains a sensitivity enhancement of 2–5× over bare QCM while keeping the fabrication-driven coefficient of variation below 0.2%, despite delivering lower absolute sensitivity than operation at the critical height. A complete sensitivity-to-uncertainty figure of merit would additionally require the dissipation and quality-factor response, which the present model does not compute, and is therefore left to future work. The uncertainty analysis also identifies pillar-height uniformity as the single most important fabrication quality target, and shows that GUM-style quadrature combination of geometric and material uncertainty is not strictly accurate near the critical height and should be replaced by a Monte Carlo approach for ACRS uncertainty budgeting.

3.7. Limitations and Assumptions

Three boundaries of the present model should be kept in view when the results above are applied. The first concerns the liquid. The fluid domain is described by the linearized Navier–Stokes equations for a Newtonian fluid, which is appropriate for the liquids used in the validation, deionized water and sucrose–water solutions up to approximately 15 cP,

and for the industrial process liquids that motivate the work. It does not extend to shear-thinning, viscoelastic, or otherwise non-Newtonian liquids. In such fluids, the shear rate imposed by the oscillating pillar varies strongly over the boundary layer and along the pillar, so the effective viscosity is not a single material constant, and the pillar motion and the fluid rheology become mutually dependent. Extending the model in this direction is in progress.

The second concerns the measured quantity. The model predicts, and the validation compares, the resonance frequency response only. Viscous losses in the liquid and viscoelastic losses in the pillar are both resolved, and they act on the predicted resonance frequency, but the model does not compute the dissipation factor D, the quality factor Q, or the motional resistance. These are device-level observables of the QCM-D measurement, and the dissipative response of the device is therefore outside the present capability of the model. Predicting that response and validating it against QCM-D measurements is the most immediate line of further work. The consequence for the present results is that every quantity reported in this work is a frequency quantity. The critical heights, the frequency-shift amplitudes, the sensitivity enhancement, the viscosity calibration and the whole of the uncertainty analysis of Section 3.6 are covered by the frequency validation of Figures 2, 3 and 5, and no result reported here depends on the dissipation factor or the quality factor.

The third concerns the scope of the uncertainty budget. The Monte Carlo analysis covers pillar height, pillar diameter, density, and Poisson ratio, which are the quantities that vary from device to device within a fabrication run. It does not include the storage modulus of the cured polymer, the liquid temperature and the density and viscosity that depend on it. The first two are controllable in practice, the storage modulus by batch characterization and temperature by instrument-level regulation, which is why they were held at nominal values. The budget reported above should therefore be read as the fabrication-driven component of the total uncertainty under temperature-controlled operation, rather than as a complete budget for field deployment. The numerical uncertainty of the finite element solution is addressed separately in Section 3.1, where it is shown to be negligible on the scale of the fabrication-driven terms.

A fourth boundary follows from the three above and concerns what this work does and does not claim to compare. The scope of the paper is the three-dimensional modeling of the ACRS device together with a fabrication- and geometry-driven uncertainty analysis, and not a full experimental uncertainty analysis of the assembled measurement system. The recommendation of sub-critical operation should be read within that scope, since it follows from the behavior of the fabrication-driven uncertainty across the operating regimes rather than from a complete experimental budget. For the same reason, a comprehensive figure of merit defined as the ratio of sensitivity to measurement uncertainty, which would permit a full comparison of the advantages and disadvantages of sub-critical ACRS against a conventional QCM, cannot be constructed here. The sensitivity term is available, since the sensitivity enhancement of Section 3.3 is already defined relative to a flat reference QCM coated with the same film, but the uncertainty term is not available on a common footing, because the dissipation and quality-factor response that such a comparison requires is not computed by the present model, and because a flat QCM carries no pillar-fabrication uncertainty term of the kind analyzed here. That comparison is therefore deferred until the dissipative response has been validated against QCM-D measurements.

4. Conclusions

This work presented a three-dimensional finite element digital twin of an advanced coupled resonance sensor (ACRS), a quartz crystal microbalance with an integrated micropillar array, operating in liquid environments. The model treats pillar height, cross-sectional shape, elastic modulus, density, internal loss factor, liquid viscosity, and liquid density as independent input parameters, and resolves the coupled fluid–structure interaction using the linearized Navier–Stokes equations in the liquid domain together with viscoelastic damping inside the pillar. The result is a parametric design tool whose architecture allows continuous exploration of the device space without physical fabrication of every configuration.

The model was validated against the pillar-height-dependent drop-and-jump response in air for square (critical height 15 μm) and circular (critical height 11 μm) pillars, against the same response in deionized water, where the critical heights shift to 13 μm and 9.5 μm, respectively, and against a sucrose–water bulk-viscosity series in which the measured frequency shift up to ~85 kHz was reproduced across the full concentration range. In all three tests, a single set of model parameters reproduced the measurements without parameter tuning between data points.

The parametric study yielded four principal findings. First, the sensitivity enhancement of the device peaks sharply near the critical height, with peak values of approximately 22.5 for square pillars and 23 for circular pillars; cross-sectional shape primarily controls the height at which the peak occurs, not its magnitude. Second, the device functions as a quantitative viscosity sensor with sub-percent precision across at least the 1–15 cP range, and does not require operation at the critical height to do so, a practical advantage given the uncertainty behavior reported below. Third, the normalized peak shear displacement reaches its maximum at the critical height for both cross-sections in air and in water, exceeding the substrate amplitude by more than an order of magnitude, and provides a unifying mechanistic picture for both sensitivity enhancement and frequency-shift amplitude. Fourth, a Monte Carlo uncertainty propagation analysis demonstrated that operation at the critical height amplifies the standard uncertainty in resonance frequency by more than an order of magnitude relative to the sub-critical regime, with geometric variability dominating over material variability by a factor of two to four. The viscosity result is validated over approximately 1–15 cP for Newtonian liquids, and this interval should be read as a boundary of the validated calibration rather than as a limit of the underlying formulation, so that use outside it constitutes extrapolation.

The principal engineering recommendation arising from this work is that ACRS devices intended for quantitative measurement should be designed and operated at sub-critical pillar heights. The sub-critical regime achieves a fabrication-driven combined coefficient of variation below 0.2% under realistic fabrication conditions and still delivers a 2–5× sensitivity enhancement over bare QCM. Operation at the critical height, while maximizing peak sensitivity, simultaneously maximizes susceptibility to fabrication variability and is therefore unsuitable for quantitative applications. From a process-development standpoint, the dominant fabrication target is pillar-height uniformity across the array, which yields a far larger reduction in measurement uncertainty than equivalent improvements in material batch consistency. The analysis also showed that standard GUM-style quadrature combination of geometric and material uncertainty is not strictly accurate near the critical height, and that Monte Carlo propagation is necessary for reliable combined uncertainty estimates in this platform.

Beyond the specific device studied here, the digital twin framework introduced in this paper provides a general methodology for the metrologically grounded design of micropillar-enhanced acoustic sensors. By treating material properties and fabrication

tolerances as first-class inputs to the simulation, the framework directly addresses the gap in the literature between physics-driven device modeling and measurement-uncertainty-driven design. Future work will extend the framework to the dissipation and quality-factor response, so that it can be validated against QCM-D measurements as well as frequency shifts; to non-Newtonian fluids, for which the linearized Navier–Stokes description used here is not valid; to an extended uncertainty budget including the storage modulus, the liquid properties and temperature; and to integration with continuous-monitoring platforms in which fluid-property drift over time is itself the primary measurement target. The framework will also be extended to close the loop between the physical device and its virtual counterpart through continuous ingestion of device data and online parameter updating, and to the construction of a comprehensive sensitivity-to-uncertainty figure of merit, which becomes possible once the dissipation and quality-factor response has been validated against QCM-D measurements.

Funding: This research received no external funding.

Data Availability Statement: The original contributions presented in this study are included in the article. Further inquiries can be directed to the corresponding author.

Conflicts of Interest: The author declares no conflicts of interest.

References

1. Voinova, M.V.; Jonson, M.; Kasemo, B. Missing mass effect in biosensor's QCM applications. *Biosens. Bioelectron.* **2002**, *17*, 835–841. [CrossRef]
2. Migoń, D.; Wasilewski, T.; Suchy, D. Application of QCM in Peptide and Protein-Based Drug Product Development. *Molecules* **2020**, *25*, 3950. [CrossRef]
3. Chowdhury, S.; Nugraha, A.S.; Yuliarto, B.; Yamauchi, Y.; Kaneti, Y.V. Nanoarchitecturing of Bimetallic Metal–Organic Frameworks for Emerging Applications in Quartz Crystal Microbalance Gas Sensors. *Small Methods* **2025**, *9*, e2401808. [CrossRef]
4. Scaccabarozzi, D.; Martina, C.; Saggin, B.; Zampetti, E. Measurement of the instrumental effect caused by flexure clamping on quartz crystal microbalances. *Appl. Sci.* **2025**, *15*, 9261. [CrossRef]
5. Rogers, N.M.K.; Herzberg, M.; Zucker, I. Using quartz crystal microbalance with dissipation monitoring to advance plastic risk assessment research. *J. Hazard. Mater. Adv.* **2025**, *18*, 100660. [CrossRef]
6. Bragazzi, N.L.; Amicizia, D.; Panatto, D.; Tramalloni, D.; Valle, I.; Gasparini, R. Quartz-crystal microbalance (QCM) for public health: An overview of its applications. *Adv. Protein Chem. Struct. Biol.* **2015**, *101*, 149–211. [CrossRef]
7. Johannsmann, D.; Langhoff, A.; Leppin, C. Studying Soft Interfaces with Shear Waves: Principles and Applications of the Quartz Crystal Microbalance (QCM). *Sensors* **2021**, *21*, 3490. [CrossRef]
8. Na Songkhla, S.; Nakamoto, T. Overview of quartz Crystal Microbalance behavior analysis and measurement. *Chemosensors* **2021**, *9*, 350. [CrossRef]
9. Scaccabarozzi, D.; Saggin, B.; Magni, M.; Corti, M.G.; Valnegri, P.; Palomba, E.; Longobardo, A.; Dirri, F.; Zampetti, E. Quartz crystal microbalances for space: De-sign and testing of a 3D printed quasi-kinematic support. *Aerospace* **2023**, *10*, 42. [CrossRef]
10. Wang, L.; Song, J.; Yu, C. The utilization and advancement of quartz crystal Microbalance (QCM): A mini review. *Microchem. J.* **2024**, *199*, 109967. [CrossRef]
11. Huang, X.; Chen, Q.; Pan, W.; Yao, Y. Advances in the Mass Sensitivity Distribution of Quartz Crystal Microbalances: A Review. *Sensors* **2022**, *22*, 5112. [CrossRef]
12. Köβlinger, C.; Uttenthaler, E.; Drost, S.; Aberl, F.; Wolf, H.; Brink, G.; Stanglmaier, A.; Sackmann, E. Comparison of the QCM and the SPR method for sur-face studies and immunological applications. *Sens. Actuators B Chem.* **1995**, *24*, 107–112. [CrossRef]
13. Naranda, J.; Bračič, M.; Vogrin, M.; Maver, U.; Trojner, T. Practical Use of Quartz Crystal Microbalance Monitoring in Cartilage Tissue Engineering. *J. Funct. Biomater.* **2022**, *13*, 159. [CrossRef]
14. Edvardsson, M.; Svedhem, S.; Wang, G.; Richter, R.; Rodahl, M.; Kasemo, B. QCM-D and reflectometry instrument: Applications to supported lipid structures and their biomolecular interactions. *Anal. Chem.* **2009**, *81*, 349–361. [CrossRef]
15. Wasilewski, T.; Szulczyński, B.; Dobrzyniewski, D.; Jakubaszek, W.; Gębicki, J.; Kamysz, W. Development and Assessment of Regeneration Methods for Peptide-Based QCM Biosensors in VOCs Analysis Applications. *Biosensors* **2022**, *12*, 309. [CrossRef]
16. Fort, A.; Landi, E.; Grasso, A.L.; Mugnaini, M.; Panzardi, E.; Vaccarella, P.; Vignoli, V. QCM measurements in Newtonian liquids: Prob-lems and performance analysis. *IEEE Trans. Instrum. Meas.* **2022**, *71*, 1–13. [CrossRef]

17. Plikusiene, I.; Maciulis, V.; Ramanavicius, A.; Ramanaviciene, A. Spectroscopic Ellipsometry and Quartz Crystal Microbalance with Dissipation for the Assessment of Polymer Layers and for the Application in Biosensing. *Polymers* **2022**, *14*, 1056. [CrossRef]
18. Nemčeková, K.; Korčeková, J.; Svitková, V.; Baraniak, D.; Domšicová, M.; Melníková, E.; Hornychová, M.; Szebellaiová, V.; Gál, M.; Poturnayová, A. Comparative Analysis of QCM and Electrochemical Aptasensors for SARS-CoV-2 Detection. *Biosensors* **2024**, *14*, 431. [CrossRef]
19. Spagnolo, S.; Muckley, E.S.; Ivanov, I.N.; Hianik, T. Application of multiharmonic QCM-D for detection of plasmin at hydrophobic surfaces modified by β-casein. *Chemosensors* **2022**, *10*, 143. [CrossRef]
20. Diltemiz, S.E.; Keçili, R.; Ersöz, A.; Say, R. Molecular Imprinting Technology in Quartz Crystal Microbalance (QCM) Sen-sors. *Sensors* **2017**, *17*, 454. [CrossRef]
21. Salazar, J.; Amer, M.; Turó, A.; Castro, N.; Navarro, M.; Soto, S.; Gabasa, Y.; López, Y.; Chávez, J.-A. Real-time detection of the bacterial biofilm formation stages using QCM-based sensors. *Chemosensors* **2023**, *11*, 68. [CrossRef]
22. Moreno, J.P.; Mertiny, P. Acoustic emission and machine learning approaches for assessing mechanical degradation in aged unidirectional glass fiber-reinforced thermoplastics. *Metrology* **2026**, *6*, 11. [CrossRef]
23. Esfahani, I.C. A data-driven physics-informed neural network for predicting the viscosity of nanofluids. *AIP Adv.* **2023**, *13*, 025206. [CrossRef]
24. Burda, I. Advanced Impedance Spectroscopy for QCM Sensor in Liquid Medium. *Sensors* **2022**, *22*, 2337. [CrossRef]
25. Wang, P.; Su, J.; Dai, W.; Cernigliaro, G.; Sun, H. Ultrasensitive quartz crystal microbalance enabled by micropillar structure. *Appl. Phys. Lett.* **2014**, *104*, 043504. [CrossRef]
26. Kashan, M.A.M.; Kalavally, V.; Lee, H.W.; Ramakrishnan, N. Resonant characteristics and sensitivity dependency on the contact surface in QCM-micropillar-based system of coupled resonator sensors. *J. Phys. D Appl. Phys.* **2016**, *49*, 195303. [CrossRef]
27. Kashan, M.A.M.; Leong, A.; Saha, T.; Kalavally, V.; Swamy, V.; Ramakrishnan, N. QCM-micropillar-based coupled resonators in the detection of gas mass flow rates. *IEEE Trans. Instrum. Meas.* **2019**, *68*, 303–305. [CrossRef]
28. Kashan, M.A.M.; Kalavally, V.; Mazumdar, P.; Lee, H.W.; Ramakrishnan, N. QCM coupled resonating systems under vacuum: Sen-sitivity and characteristics. *IEEE Sens. J.* **2017**, *17*, 5044–5049. [CrossRef]
29. Esfahani, I.C.; Ji, S.; Sun, H. A drop-on-micropillars (DOM)-based acoustic wave viscometer for high viscosity liquid measurement. *IEEE Sens. J.* **2023**, *23*, 24224–24230. [CrossRef]
30. Kashan, M.A.M.; Kalavally, V.; Ramakrishann, N. Investigation into methods for tuning QCM-pillar system of coupled resonator sensors. In Proceedings of the 2016 IEEE International Symposium on Robotics and Intelligent Sensors (IRIS), Tokyo, Japan, 17–20 December 2016; pp. 168–171.
31. Esfahani, I.C.; Tehrani, N.A.; Ji, S.; Sun, H. Simultaneous Protein Adsorption and Viscosity Measurement using Micropillar-Enhanced Acoustic Wave (μPAW) Device for Pharmaceutical Applications. *J. Pharm. Sci.* **2024**, *113*, 2715–2722. [CrossRef]
32. Esfahani, I.C.; Tehrani, N.A.; Yang, R.; Xiang, X.; Sun, H. Real-Time Wetting Area Measurement of Micro- and Nanostructured Surfaces with an Acoustic Wave Device. *Langmuir* **2025**, *41*, 27350–27359. [CrossRef]
33. Losada-Pérez, P.; Polat, O.; Parikh, A.N.; Seker, E.; Renner, F.U. Engineering the interface between lipid membranes and nanopo-rous gold: A study by quartz crystal microbalance with dissipation monitoring. *Biointerphases* **2018**, *13*, 011002. [CrossRef]
34. Jonsson, M.P.; Jönsson, P.; Dahlin, A.B.; Höök, F. Supported lipid bilayer formation and lipid-membrane-mediated biorecognition reactions studied with a new nanoplasmonic sensor template. *Nano Lett.* **2007**, *7*, 3462–3468. [CrossRef]
35. Dahlin, A.B.; Jönsson, P.; Jonsson, M.P.; Schmid, E.; Zhou, Y.; Höök, F. Synchronized quartz crystal microbalance and nanoplas-monic sensing of biomolecular recognition reactions. *ACS Nano* **2008**, *2*, 2174–2182. [CrossRef]
36. Wang, P.; Su, J.; Su, C.-F.; Dai, W.; Cernigliaro, G.; Sun, H. An ultrasensitive quartz crystal microbalance-micropillars based sensor for humidity detection. *J. Appl. Phys.* **2014**, *115*, 224501. [CrossRef]
37. Mohaidat, S.; Okour, M.; Al Fayad, M.; Alsaleem, F. High-frequency coupled-resonator CMUT with stepped cavity for enhanced sensitivity and bandwidth in acoustic emission detection. *Metrology* **2026**, *6*, 29. [CrossRef]
38. Tsuboi, H.; Kaizuka, T.; Shirai, K. Effect of dispersed particle concentration on photoacoustic flowmetry using low-frequency transducers. *Metrology* **2025**, *5*, 79. [CrossRef]
39. Kok, G.; van Dijk, M. Measurement uncertainty evaluation: Differences between virtual experiments and the standardized approach. *Metrology* **2025**, *5*, 59. [CrossRef]
40. Rodríguez-Rama, J.A.; Madrigal, L.P.; Lázaro, A.M.; Lorenzo, J.M.; Laso, A.G.; Mustelier, J.L.C.; Martín-Sánchez, D.A. Metrological validation of low-cost DS18B20 digital temperature sensors using the TH-001 procedure: Calibration models, uncertainty, and reproducibility. *Metrology* **2026**, *6*, 21. [CrossRef]
41. Oo, T.P.; Phakaew, T.; Uzair, M.; Akkaraekthalin, P.; Jeamsaksiri, W.; Chalermwisutkul, S. A cost-effective cylindrical capacitive sensor for liquid dielectric characterization from 1 to 30 MHz. *Metrology* **2026**, *6*, 23. [CrossRef]
42. Della Giovanna, L.; Guastavino, F.; Torello, E. Experimental study of High-frequency current transformer for partial discharge detection using frequency and impulse metrics. *Metrology* **2026**, *6*, 24. [CrossRef]

43. Esfahani, I.C.; Sun, H. A droplet-based micropillar-enhanced acoustic wave (μPAW) device for viscosity measurement. *Sens. Actuators A Phys.* **2023**, *350*, 114121. [CrossRef]
44. Esfahani, I.C.; Ji, S.; Tehrani, N.A.; Sun, H. An ultrasensitive micropillar-enabled acoustic wave (μPAW) microdevice for real-time viscosity measurement. *Microsyst. Technol.* **2023**, *29*, 1631–1641. [CrossRef]

Disclaimer/Publisher's Note: The statements, opinions and data contained in all publications are solely those of the individual author(s) and contributor(s) and not of MDPI and/or the editor(s). MDPI and/or the editor(s) disclaim responsibility for any injury to people or property resulting from any ideas, methods, instructions or products referred to in the content.